Physica B 615 (2021) 412992

Contents lists available at ScienceDirect

Physica B: Physics of Condensed Matter

journal homepage: http://www.elsevier.com/locate/physb

Transverse spin polarization of a Rashba-Zeeman-coupled Fermi superfluid

M. Iskin

Department of Physics, Koç University, Rumelifeneri Yolu, 34450, Sarıyer, Istanbul, Turkey

ARTICLE INFO

Keywords:
BCS-BEC crossover
Rashba spin-orbit coupling
Spin polarization
Bulk-boundary correspondence

ABSTRACT

We apply the Bogoliubov-de Gennes theory to a superfluid Fermi gas that is confined to a disc, and analyze its transverse spin polarization that is produced by the simultaneous presence of an out-of-plane Zeeman field and an in-plane Rashba spin-orbit coupling. This is a finite-size effect whose physical origin is directly associated with the equilibrium mass-current density. Our numerical findings for the ground state suggest a bulk-boundary correspondence between characteristic features of the edge-bound transverse polarization and the changes in the momentum-space topology of the bulk.

1. Introduction

Thanks to the experimental realizations of a variety of synthetic spin-orbit coupling (SOC) schemes with atomic Fermi gases [1–5], there has been a surge of theoretical proposals on how the strength and symmetry of the SOC affects a Fermi gas, e.g, see the following reviews [6–11]. In the context of superfluid (SF) Fermi gases, most of the recent works has been focused on the thermodynamic phase diagram of infinite systems, including the stability of topologically-nontrivial SF phases and the enhancement of the Fulde-Ferrel-Larkin-Ovchinnikov (FFLO)-type modulating SF phases throughout the BCS-BEC evolution. It is also remarkable that the BCS-BEC evolution can be equivalently realized by either changing the *s*-wave scattering length through a Feshbach resonance or increasing the strength of SOC when the SOC field has more than one component. Unfortunately, despite a number of attempts, the observation of many-body effects still suffers from the heating that is caused by the lasers, and there is a continuous search for alternative SOC schemes.

There are also theoretical proposals for SOC-induced novel phenomena that appear only in finite-size systems. For instance, in one of our earlier works [12], where a spin-orbit-coupled Fermi gas is confined to a harmonically-trapped optical lattice, we inadvertently found that its spin polarization is not necessarily aligned with the Zeeman field. In addition to the usual longitudinal component, there also appears an edge-bound transverse component whose origin can be traced back to the equilibrium currents and topological transitions. Furthermore, depending on the directions of the Zeeman and SOC fields, no matter how weak their strengths are, the transverse polarization not only modulates in space but also exhibits intriguing polarization textures [12]. We note that similar results have recently been proposed for one-dimensional systems as well in the context of Majorana nanowires [13–15]. Even though the resultant polarization textures were thoroughly examined in our earlier work [12], their physical mechanism was somewhat hindered by the presence of both the tight-binding lattice model and the harmonic confinement. The remaining question is whether the transverse polarization can be used as a probe for equilibrium mass currents and topological transitions or not. Motivated also by the recent interest in related problems in the condensed-matter community [13–15], here we overcome these difficulties by analyzing a continuum model in a disc, and attribute some of our new findings directly to a bulk-boundary correspondence. In addition, we consider an in-plane Rashba SOC and an out-of-plane Zeeman field, and take advantage of the radial symmetry.

The rest of the paper is organized as follows. In Sec. 2, we first introduce the mean-field Hamiltonian density, and then derive a set of self-consistency equations through the Bogoliubov-de Gennes (BdG) formalism [16]. In App. A, we review the numerical implementation of these BdG equations to an SF Fermi gas that is confined to a finite disc, and present its numerical results in Sec. 3. We also obtain the bulk phase diagrams in Sec. 3 through the BCS-BEC mean-field theory for an infinite system that is briefly reviewed in App. B. The paper ends with a brief summary of our conclusions and an outlook in Sec. 4.

2. Bogoliubov-de Gennes equations

In the presence of an isotropic in-plane SOC in the xy plane, the mean-field Hamiltonian density can be written as

E-mail address: miskin@ku.edu.tr.

https://doi.org/10.1016/j.physb.2021.412992
Received 16 December 2020; Accepted 16 March 2021
Available online 25 March 2021

$$H_{mf}(\mathbf{r}) = \sum_{\sigma,\sigma'} \psi^\dagger_\sigma(\mathbf{r}) K_{\sigma\sigma'}(\mathbf{r}) \psi_{\sigma'}(\mathbf{r}) + \Delta(\mathbf{r}) \psi^\dagger_\uparrow(\mathbf{r}) \psi^\dagger_\downarrow(\mathbf{r}) + \Delta^*(\mathbf{r}) \psi_\downarrow(\mathbf{r}) \psi_\uparrow(\mathbf{r}), \quad (1)$$

where $\psi^\dagger_\sigma(\mathbf{r})$ creates a spin $\sigma = \{\uparrow, \downarrow\}$ fermion at position $\mathbf{r}$, $K_{\sigma\sigma}(\mathbf{r}) = -\nabla^2/(2\,\mathrm{M}) - \mu_\sigma$ is the kinetic energy (in units of $\hbar = 1$) of fermions with mass M and it is shifted by the chemical potential μ_σ, $K_{\uparrow\downarrow}(\mathbf{r}) = K^\dagger_{\downarrow\uparrow}(\mathbf{r}) = \alpha(p_y + ip_x)$ is the SOC with strength $\alpha \geq 0$ and momentum operator $p_j = -i\partial/\partial j$, and $\Delta(\mathbf{r})$ is the SF order parameter. To diagonalize this Hamiltonian, we introduce the Bogoliubov-Valatin transformation $\psi_\sigma(\mathbf{r}) = \sum_n [u_{\sigma n}(\mathbf{r})\gamma_n + v^*_{\sigma n}(\mathbf{r})\gamma^\dagger_n]$, where $\gamma^\dagger_n$ creates a spin σ quasiparticle in state n [16]. As a result, we obtain the BdG equation $H_{\mathrm{BdG}}(\mathbf{r})\phi_n(\mathbf{r}) = \epsilon_n \phi_n(\mathbf{r})$, where the Hamiltonian matrix

$$H_{\mathrm{BdG}}(\mathbf{r}) = \begin{bmatrix} K_{\uparrow\uparrow}(\mathbf{r}) & K_{\uparrow\downarrow}(\mathbf{r}) & 0 & \Delta(\mathbf{r}) \\ K_{\downarrow\uparrow}(\mathbf{r}) & K_{\downarrow\downarrow}(\mathbf{r}) & -\Delta(\mathbf{r}) & 0 \\ 0 & -\Delta^*(\mathbf{r}) & -K^*_{\uparrow\uparrow}(\mathbf{r}) & -K^*_{\uparrow\downarrow}(\mathbf{r}) \\ \Delta^*(\mathbf{r}) & 0 & -K^*_{\downarrow\uparrow}(\mathbf{r}) & -K^*_{\downarrow\downarrow}(\mathbf{r}) \end{bmatrix} \quad (2)$$

is expressed in the spinor basis $\phi_n(\mathbf{r}) = [u_{\uparrow n}(\mathbf{r}), u_{\downarrow n}(\mathbf{r}), v_{\uparrow n}(\mathbf{r}), v_{\downarrow n}(\mathbf{r})]^{\mathrm{T}}$ with T the transpose, and $\epsilon_n \geq 0$ is the corresponding energy eigenvalue.

For a self-consistent solution of Eq. (2), we reexpress the order parameter $\Delta(\mathbf{r}) = g\langle\psi_\uparrow(\mathbf{r})\psi_\downarrow(\mathbf{r})\rangle$ as

$$\Delta(\mathbf{r}) = g\sum_n \left[u_{\uparrow n}(\mathbf{r}) v^*_{\downarrow n}(\mathbf{r}) f(\epsilon_n) + u_{\downarrow n}(\mathbf{r}) v^*_{\uparrow n}(\mathbf{r}) f(-\epsilon_n)\right], \quad (3)$$

where $g \geq 0$ is the strength of the local attraction between fermions, $\langle\cdots\rangle$ is the thermal average, and $f(x) = 1/(e^{x/T} + 1)$ is the Fermi distribution with T the temperature (in units of $k_{\mathrm{B}} = 1$). In addition, we reexpress the local density of fermions $n_\sigma(\mathbf{r}) = \langle\psi^\dagger_\sigma(\mathbf{r})\psi_\sigma(\mathbf{r})\rangle$ as

$$n_\sigma(\mathbf{r}) = \sum_n [|u_{\sigma n}(\mathbf{r})|^2 f(\epsilon_n) + |v_{\sigma n}(\mathbf{r})|^2 f(-\epsilon_n)], \quad (4)$$

and determine μ_σ through the number equation $N_\sigma = \int d^2\mathbf{r} n_\sigma(\mathbf{r})$ Since the mean-field theory works best at low temperatures, below we apply it only to the ground state of the system, and set $T = 0$.

Our main interest is in the spin polarization $\mathbf{P}(\mathbf{r}) = \langle\Psi^\dagger(\mathbf{r})\boldsymbol{\sigma}(\mathbf{r})\Psi(\mathbf{r})\rangle$ of the Fermi gas where $\Psi(\mathbf{r}) = [\,\psi_\uparrow(\mathbf{r}) \quad \psi_\downarrow(\mathbf{r})\,]^{\mathrm{T}}$. Its projection onto the x axis is $P_x(\mathbf{r}) = 2\mathrm{Re}\langle\psi^\dagger_\uparrow(\mathbf{r})\psi_\downarrow(\mathbf{r})\rangle$ with Re the real part, onto the y axis is $P_y(\mathbf{r}) = 2\mathrm{Im}\langle\psi^\dagger_\uparrow(\mathbf{r})\psi_\downarrow(\mathbf{r})\rangle$ with Im the imaginary part, and onto the z axis is $P_z(\mathbf{r}) = \langle\psi^\dagger_\uparrow(\mathbf{r})\psi_\uparrow(\mathbf{r})\rangle - \langle\psi^\dagger_\downarrow(\mathbf{r})\psi_\downarrow(\mathbf{r})\rangle$. Note that $P_z(\mathbf{r}) = n_\uparrow(\mathbf{r}) - n_\downarrow(\mathbf{r})$ is the longitudinal (out-of-plane) polarization along the effective Zeeman field, and $\boldsymbol{P}_\perp(\mathbf{r}) = P_x(\mathbf{r})\hat{\mathbf{x}} + P_y(\mathbf{r})\hat{\mathbf{y}}$ is the transverse (in-plane) polarization induced by SOC. Alternatively, we introduce $P_\perp(\mathbf{r}) = P_x(\mathbf{r}) + iP_y(\mathbf{r})$, and reexpress it as

$$P_\perp(\mathbf{r}) = 2\sum_n [u^*_{\uparrow n}(\mathbf{r}) u_{\downarrow n}(\mathbf{r}) f(\epsilon_n) + v_{\uparrow n}(\mathbf{r}) v^*_{\downarrow n}(\mathbf{r}) f(-\epsilon_n)]. \quad (5)$$

Having derived the BdG equations, next we apply them for an SF Fermi gas that is confined to a disc of radius R at $T = 0$.

3. Fermi gas confined to a disc

The numerical procedure is discussed in App. A, where the BdG Eqs. (2)–(5) are projected onto a set of Bessel functions that are normalized in a disc of radius R. We iterate the resultant equations until they converge to a self-consistent solution, and use two benchmarks to make sure of the numerical implementation of the BdG equations. First we checked that our BdG theory for the disc and BCS-BEC theory for the infinite system are in good agreement with each other for the $h_z = \Delta(0)$ and $h_z = \sqrt{\Delta^2(0) + \mu^2}$ boundaries discussed below in the analysis of the figures, where $h_z = (\mu_\uparrow - \mu_\downarrow)/2$ is the effective Zeeman field and $\mu = (\mu_\uparrow + \mu_\downarrow)/2$ is the average chemical potential. Second we checked that a pair of edge-bound Majorana states appear for the disc when $h_z > \sqrt{\Delta^2(0) + \mu^2}$.

As an illustration, Fig. 1 shows typical modulations of $P_\perp(r)$ near the edge of the disc, where the positive (negative) regions indicate a radially outward (inward) transverse polarization, i.e., $\boldsymbol{P}_\perp(\mathbf{r}) = P_\perp(r)\hat{\mathbf{r}}$ where $P_\perp(\mathbf{r}) = e^{i\theta}P_\perp(r)$ is given by Eq. (5). First of all we note that $P_\perp(r)$ tends rapidly to 0 towards the center of the disc when $r \to 0$. This is not surprising given that $\boldsymbol{P}_\perp(\mathbf{r})$ is precisely $\mathbf{0}$ in an infinite system, and its nontrivial modulation near the edge of the disc is a finite-size effect that is caused by the simultaneous presence of a Zeeman field and Rashba SOC, no matter how weak they are [12].

One way to understand the physical origin of the edge-induced transverse polarization is through its relation to the equilibrium mass-current density $\mathbf{J}(\mathbf{r})$ [17]. Using the continuity equation $\partial n(\mathbf{r})/\partial t + \nabla\cdot\mathbf{J}(\mathbf{r}) = 0$ with $n(\mathbf{r}) = \sum_\sigma n_\sigma(\mathbf{r})$ the local density of fermions, it can be shown that $\mathbf{J}(\mathbf{r}) = J_\theta(r)\hat{\boldsymbol{\theta}}$ has a nonvanishing component in the azimuthal direction that is given by two contributions $J_\theta(r) = \sum_\sigma J_\sigma(r) + J_{\uparrow\downarrow}(r)$. While the first term is the usual contribution, the second term $J_{\uparrow\downarrow}(r) = \alpha P_\perp(r)$ is caused by SOC and it is proportional to $P_\perp(r)$. This suggests that the transverse polarization is directly associated with the mass-current density that is induced by the broken time-reversal symmetry of the system in the presence of a SOC. In the context of nanowires with SOC [13–15], it has been recently shown that a bulk equilibrium spin current manifests itself in a sizable edge spin polarization transverse to the Zeeman field as well.

Alternatively, the microscopic origin of the transverse polarization near the edge of the disc can also be traced back to the changes in the momentum-space topology of its bulk near the center of the disc. Such a bulk-boundary correspondence is suggested by our numerical results that are shown in Figs. 2(a) and 3(a) and 4. Here the bulk phase diagrams P_z/N vs. $m\alpha/k_{\mathrm{F}}$ are obtained through an independent calculation by solving the BCS-BEC mean-field theory for an infinite system [18]. See App. B for a brief review of the theory and the physical significance of the black-dotted $h_z = \sqrt{\Delta^2 + \mu^2}$ and $h_z = \Delta$ lines. The SF phase is known to be topological above the $h_z = \sqrt{\Delta^2 + \mu^2}$ line. In Figs. 2(a), 3(a) and 4, the red-dotted lines are determined by our BdG theory. i.e., for a given $m\alpha/k_{\mathrm{F}}$ each dot corresponds to the location of the maximum $P_\perp/N$ that is extracted from Figs. 2(b) or 3(b). Since $P_\perp(r)$ oscillates in space, here we use $P_\perp = \int d^2\mathbf{r} P_\perp(r)$ as the strength of the total transverse polarization [13–15], and use $P_z = \int d^2\mathbf{r} P_z(r)$ to determine the population imbalance between $\uparrow$ and $\downarrow$ fermions. Note that $h_z \geq 0$ leads to an isotropic $P_z(\mathbf{r}) = P_z(r) \geq 0$ for all r.

In the weak-SOC limit when $m\alpha/k_{\mathrm{F}} \ll 1$, Figs. 2(c) and 3(c) show that $P_\perp$ increases linearly with h_z and exhibits a sharp cusp at $h_z \approx \Delta(0)$, where $\Delta(0)$ is the bulk order parameter at the center of the disc. Given the similar findings on nanowires [13–15], we suspect these cusps are caused by the change in the momentum-space topology of the bulk that is discussed in App. B. Up to a high precision, we indeed find that our BdG results for the location of the cusp coincide quite well with those of the BCS-BEC meanfield theory for $h_z = \Delta$ when $m\alpha/k_{\mathrm{F}} \to 0$ is small. This is best seen in Figs. 3(a) and 4 when $\epsilon_b/\epsilon_F \ll 1$, but not in Fig. 2(a) where ϵ_b/ϵ_F is large. The latter disagreement is caused by the instability of the bulk towards phase separation, and can be explained as follows. Our bulk phase diagram shown in Fig. 2(a) is known to be unreliable in the $m\alpha/k_{\mathrm{F}} \lesssim 0.3$ region due to an instability towards phase separation. We refer the reader to Fig. 1 of Ref. [18] for a more accurate phase diagram of the same system, including the boundary for the phase-separated region. They showed that the phase separation gradually becomes important when ϵ_b/ϵ_F is increased from 0. In agreement with this insight provided by the BCS-BEC theory for an infinite system [18], we find that the bulk of the BdG result for the disc is also not uniform, and therefore, the bulk-boundary correspondence with $\Delta(0)$ looses its meaning when ϵ_b/ϵ_F is not small. Furthermore, Figs. 2(b) and 3(b) show that $P_\perp$ rises so steeply with P_z that it eventually exceeds P_z when $m\alpha/k_{\mathrm{F}} \to 0$. This is

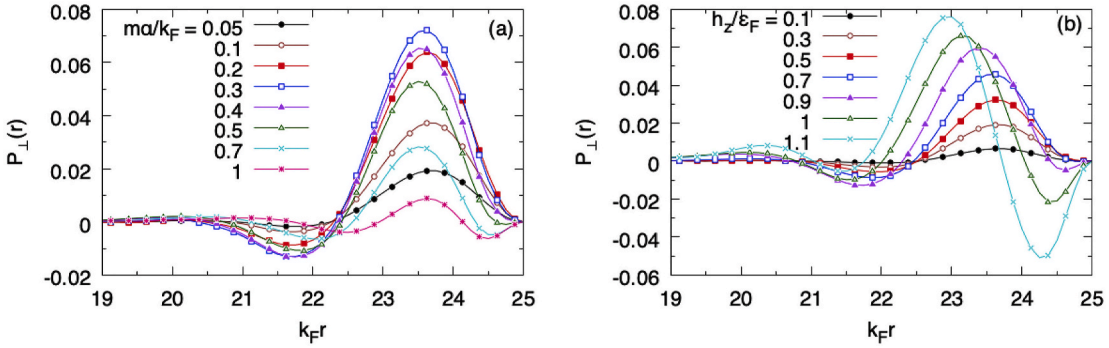

Fig. 1. Transverse polarization $P_\perp(r)$ [in units of $k_F^2/(2\pi)$] as a function of r, where $h_z = 0.8\epsilon_F$ in (a), $\alpha = 0.5\ k_F/M$ in (b), and $\epsilon_b = 0.6\epsilon_F$ in both.

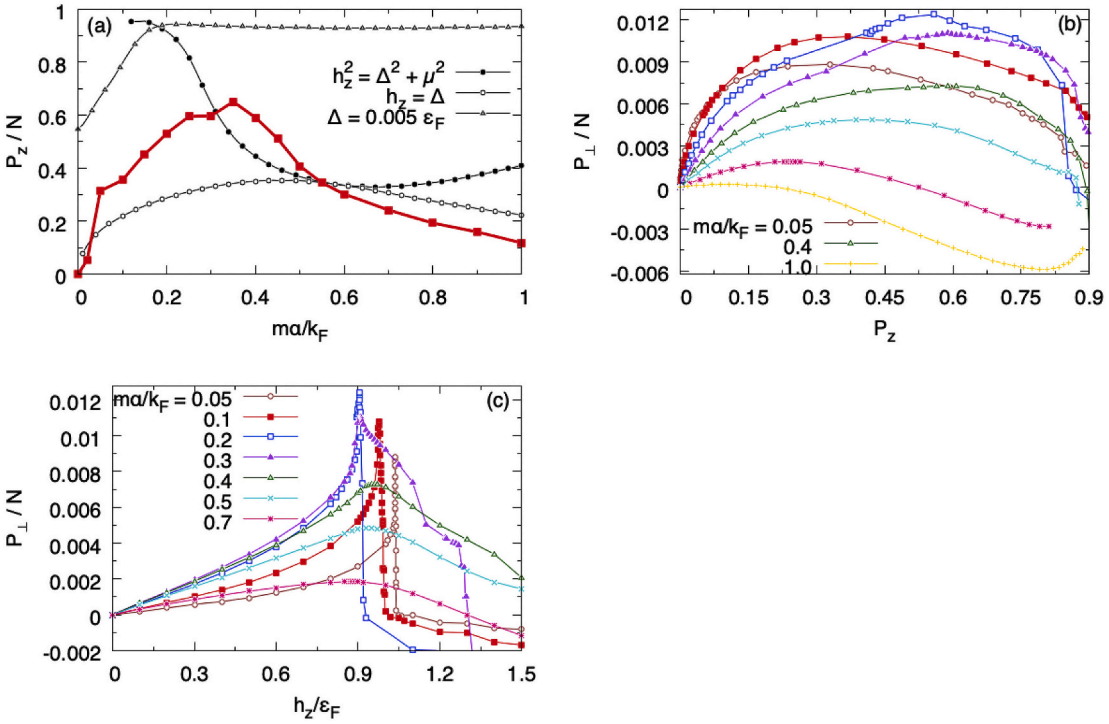

Fig. 2. (a) The bulk phase diagram is obtained through an independent calculation by solving the BCS-BEC mean-field theory for an infinite system, and the red-dotted line in (a) corresponds to the locations of the maximum $P_\perp/N$ that are extracted from (b). Figures (b) and (c) are color-coded, i.e., the same colors represent the same data. Here the two-body binding energy $\epsilon_b = 0.6\epsilon_F$ is fixed and the Zeeman field h_z is varied for every given SOC $m\alpha/k_F$. In (a), the SF phase is topological above the $h_z = \sqrt{\Delta^2 + \mu^2}$ line, and the $\Delta = 0.005\epsilon_F$ line is shown as a guide to the eye for the SF-Normal phase transition boundary. (For interpretation of the references to color in this figure legend, the reader is referred to the Web version of this article.)

quite intriguing given that $P_\perp$ is induced by h_z, and therefore P_z, to start with.

When $m\alpha/k_F$ is gradually increased, Figs. 2(c) and 3(c) show that the peak of $P_\perp$ first goes up, then broadens, and then goes down. This is in such a way that $P_\perp$ eventually changes sign and becomes negative as shown in Figs. 2(b) and 3(b). In addition, Figs. 2(a), 3(a) and 4 show that the location of the maximum $P_\perp$ (i.e., the red-dotted lines in those figures) first rises up with the SF-Normal transition boundary that is guided approximately by the $\Delta = 0.005\epsilon_F$ line. Just after it crosses the topological transition boundary that is given by the $h_z = \sqrt{\Delta^2(0) + \mu^2}$ line, it bends down towards 0 following closely the topological transition boundary until μ changes sign. In all of our trials, we find that the red-dotted line and the topological transition boundary meet precisely when $\mu = 0$, beyond which the latter line immediately bends upwards. We note that the effective Fermi surface disappears entirely in the latter regime when $\mu \leq 0$. We believe such correlations between the transverse polarization of an SF Fermi gas near its edges and the changes in the momentum-space topology of its bulk offer further evidence for the existence of a bulk-boundary correspondence in between. Unfortunately, due to our limited computational resources, the question remains whether the peak of the transverse polarization occurs precisely at $h_z \to \sqrt{\Delta^2(0) + \mu^2}$ in a larger disc when $k_F R \to \infty$.

4. Conclusion

In summary, we used the mean-field BdG theory to analyze the edge-bound transverse spin polarization of an SF Fermi gas that is confined to a disc of radius R at zero temperature. This a finite-size effect that is induced by the simultaneous presence of an out-of-plane Zeeman field (h_z) and an in-plane SOC, no matter how weak they are. We first related its physical origin directly to the equilibrium mass-current density, and

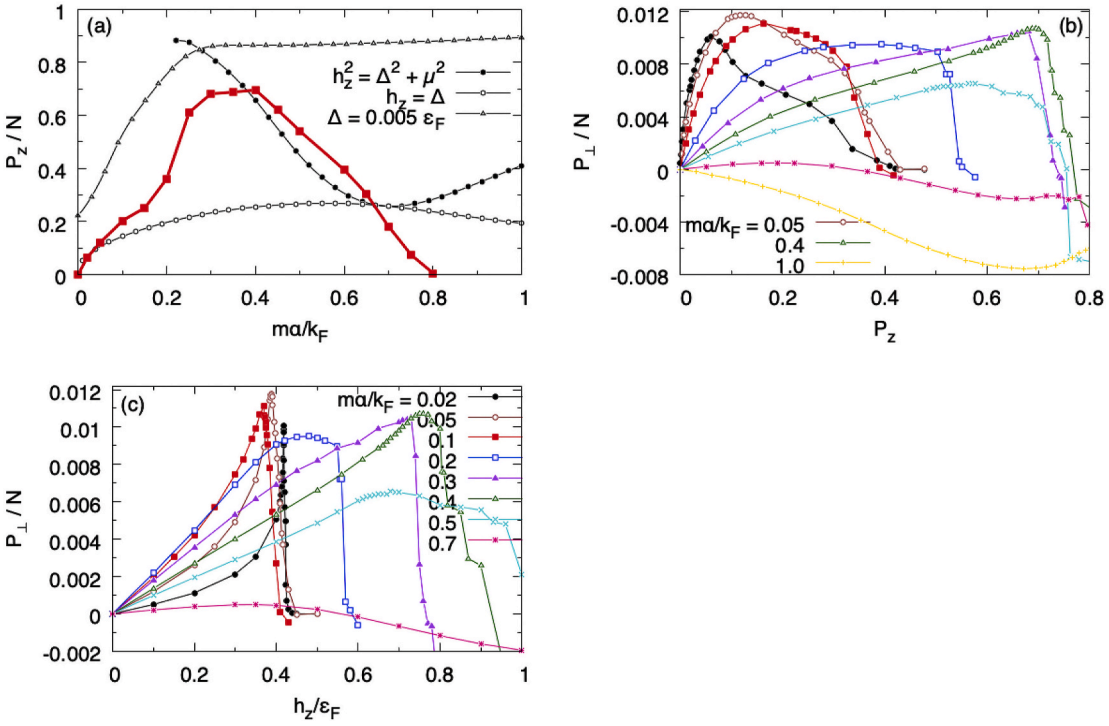

Fig. 3. Same as in Fig. 2 but for $\epsilon_b = 0.1\epsilon_F$.

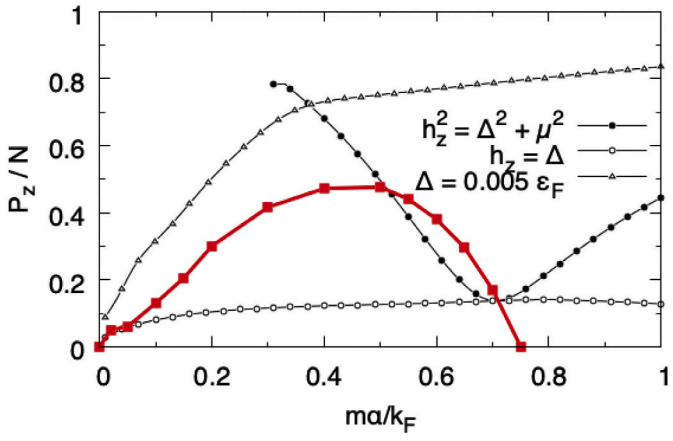

Fig. 4. Same as in Fig. 2(a) but for $\epsilon_b = 0.01\epsilon_F$.

then attributed some of its characteristic features to the bulk properties of an SF Fermi gas. In particular, as long as there exists an effective Fermi surface with a positive chemical potential ($\mu \geq 0$), we found that while the total transverse polarization ($P_\perp$) exhibits a sharp cusp around $h_z \approx \Delta(0)$ in the weak-SOC regime, it exhibits a broad peak nearby $h_z \sim \sqrt{\Delta^2(0) + \mu^2}$ in the large-SOC regime until μ changes sign. We believe such correlations between the $P_\perp$ of an SF Fermi gas near its edges and the changes in the momentum-space topology of its bulk offer some evidence for the existence of a bulk-boundary correspondence in between. Therefore, similar to the theoretical proposals for the nanowires [13–15], it may be possible to use the transverse polarization as a probe for equilibrium mass currents and topological transitions in higher dimensions as well. As an outlook, it is worthwhile to check whether the transverse polarization exhibits a peak precisely at $h_z \to \sqrt{\Delta^2(0) + \mu^2}$ or not as a function of increasing R, and to analyze it for other confined geometries.

Declaration of competing interest

I declare no conflict of interest.

Acknowledgements

The author thanks Ahmet Keleş for discussions, and acknowledges funding from Scientific and Technological Research Council of Turkey (TÜBİTAK) Grant No. 11001-118F359.

Appendix A. BdG equations for an SF Fermi gas that is confined to a disc

Assuming that the SF Fermi gas is confined to a disc of radius R, and adopting the polar $\mathbf{r} = (r, \theta)$ coordinate system, we decouple the BdG equations into independent angular momentum (m) sectors by choosing $u_{\uparrow n}(\mathbf{r}) = u_{\uparrow nm}(r)e^{im\theta}/\sqrt{2\pi}$ with $u_{\uparrow nm}(r) = \sum_j c_{\uparrow nmj}\varphi_{j,m}(r)$, and $v_{\uparrow n}(\mathbf{r}) = v_{\uparrow nm}(r)e^{i(m+1)\theta}/\sqrt{2\pi}$ with $v_{\uparrow nm}(r) = \sum_j d_{\uparrow nmj}\varphi_{j,m+1}(r)$ for the $\uparrow$ components; and $u_{\downarrow n}(\mathbf{r}) = u_{\downarrow nm}(r)e^{i(m+1)\theta}/\sqrt{2\pi}$ with $u_{\downarrow nm}(r) = \sum_j c_{\downarrow nmj}\varphi_{j,m+1}(r)$, and $v_{\downarrow n}(\mathbf{r}) = v_{\downarrow nm}(r)e^{im\theta}/\sqrt{2\pi}$ with $v_{\downarrow nm}(r) = \sum_j d_{\downarrow nmj}\varphi_{j,m}(r)$ for the $\downarrow$ ones. Here, since the radial wave functions are projected onto a set of Bessel functions that are normalized in a disc of radius R, i.e. $\varphi_{j,m}(r) = \sqrt{2}J_m(\beta_{j,m}r/R)/[RJ_{m+1}(\beta_{j,m})]$, where $j = 1, 2, 3, \ldots$and the argument $\beta_{j,m}$ is the jth zero of $J_m(x)$, they automatically satisfy the boundary conditions $u_{\sigma nm}(R) = v_{\sigma nm}(R) = 0$ on the periphery of the disc [19].

Given the orthonormality condition $\int_0^R rdr\varphi_{j,m}(r)\varphi_{j',m}(r)=\delta_{jj'}$ with $\delta_{jj'}$ the Kronecker delta, and allowing $1\le j\le j_{max}$ states, the BdG equation is reduced to a $4j_{max}\times 4j_{max}$ matrix eigenvalue problem,

$$\sum_{j'}\begin{pmatrix} K^{jj'}_{\uparrow,m} & S^{jj'}_{m} & 0 & \Delta^{jj'}_{m} \\ S^{j'j}_{m} & K^{jj'}_{\downarrow,m+1} & -\Delta^{jj'}_{m+1} & 0 \\ 0 & -\Delta^{jj'}_{m+1} & -K^{jj'}_{\uparrow,m+1} & S^{j'j}_{m} \\ \Delta^{jj'}_{m} & 0 & S^{jj'}_{m} & -K^{jj'}_{\downarrow,m} \end{pmatrix}\begin{pmatrix} c_{\uparrow nmj'} \\ c_{\downarrow nmj'} \\ d_{\uparrow nmj'} \\ d_{\downarrow nmj'} \end{pmatrix}=\epsilon_{nm}\begin{pmatrix} c_{\uparrow nmj} \\ c_{\downarrow nmj} \\ d_{\uparrow nmj} \\ d_{\downarrow nmj} \end{pmatrix}, \tag{A.1}$$

for each m. Here, the matrix elements are given by $K^{jj'}_{\sigma,m}=[\beta^2_{j,m}/(2\,MR^2)-\mu_\sigma]\delta_{jj'}$ for the kinetic energy terms, $S^{jj'}_{m}=\alpha\int_0^R rdr\varphi_{j,m}(r)[\partial/\partial r+(m+1)/r]\varphi_{j',m+1}(r)$ for the SOC ones leading to $S^{jj'}_{m}=-S^{j'j}_{-m-1}=-(2\alpha/R)\beta_{j,m}\beta_{j',m+1}/(\beta^2_{j,m}-\beta^2_{j',m+1})$, and $\Delta^{jj'}_{m}=\int_0^R rdr\Delta(r)\varphi_{j,m}(r)\varphi_{j',m}(r)$ for the pairing ones. Here we assume $\Delta(r)$ is real without losing generality.

Similarly, the order-parameter equation reduces to

$$\Delta(r)=\frac{g}{2\pi}\sum_{nmjj'}[c_{\downarrow nmj}d_{\uparrow nmj'}\varphi_{j,m+1}(r)\varphi_{j',m+1}(r)f(\epsilon_{nm})+c_{\uparrow nmj}d_{\downarrow nmj'}\varphi_{j,m}(r)\varphi_{j',m}(r)f(-\epsilon_{nm})], \tag{A.2}$$

and the local-density equations reduce to

$$n_\uparrow(r)=\frac{1}{2\pi}\sum_{nmjj'}[c_{\uparrow nmj}c_{\uparrow nmj'}\varphi_{j,m}(r)\varphi_{j',m}(r)f(\epsilon_{nm})+d_{\uparrow nmj}d_{\uparrow nmj'}\varphi_{j,m+1}(r)\varphi_{j',m+1}(r)f(-\epsilon_{nm})], \tag{A.3}$$

$$n_\downarrow(r)=\frac{1}{2\pi}\sum_{nmjj'}[c_{\downarrow nmj}c_{\downarrow nmj'}\varphi_{j,m+1}(r)\varphi_{j',m+1}(r)f(\epsilon_{nm})+d_{\downarrow nmj}d_{\downarrow nmj'}\varphi_{j,m}(r)\varphi_{j',m}(r)f(-\epsilon_{nm})]. \tag{A.4}$$

Note that the total number of fermions is simply given by $N_\sigma=\sum_{nmj}[c^2_{\sigma nmj}f(\epsilon_{nm})+d^2_{\sigma nmj}f(-\epsilon_{nm})]$. In addition, the transverse polarization $\boldsymbol{P}_\perp(\mathbf{r})=P_\perp(r)\hat{\mathbf{r}}$ is in the radial direction with $P_\perp(\mathbf{r})=e^{i\theta}P_\perp(r)$, and its projection onto the r axis is

$$P_\perp(r)=\frac{1}{\pi}\sum_{nmjj'}[c_{\uparrow nmj}c_{\downarrow nmj'}\varphi_{j,m}(r)\varphi_{j',m+1}(r)f(\epsilon_{nm})+d_{\uparrow nmj}d_{\downarrow nmj'}\varphi_{j,m+1}(r)\varphi_{j',m}(r)f(-\epsilon_{nm})]. \tag{A.5}$$

Here, and throughout, all of the sums are restricted to positive energy $0\le\epsilon_{nm}\le\epsilon_c$ eigenstates up to a cutoff energy ϵ_c. Limiting our numerical calculations to zero temperature, we choose $\epsilon_c=10k_F^2/(2\,M)$ and $R=25/k_F$ with $N=(k_FR)^2/2$, and $j_{max}=50$ and $|m|_{max}=75$. In addition, we follow the usual convention, and relate g to the two-body binding energy $\epsilon_b\ge 0$ of fermions in vacuum through the relation $g=4\pi/[M\log(1+2\epsilon_c/\epsilon_b)]$.

Appendix B. BCS-BEC meanfield theory for an infinite system

In the case of an infinite system, we adopt a momentum-space ($\mathbf{k}$) formulation, and express the self-consistency (order parameter and number) equations compactly as [20].

$$\frac{1}{g}=\frac{1}{2}\sum_{\mathbf{k},s}\frac{\partial E_{\mathbf{k},s}}{\partial\Delta^2}\tanh\left(\frac{E_{\mathbf{k},s}}{2T}\right), \tag{B.1}$$

$$N_\uparrow+N_\downarrow=\frac{1}{2}\sum_{\mathbf{k},s}\left[1+\frac{\partial E_{\mathbf{k},s}}{\partial\mu}\tanh\left(\frac{E_{\mathbf{k},s}}{2T}\right)\right], \tag{B.2}$$

$$N_\uparrow-N_\downarrow=\frac{1}{2}\sum_{\mathbf{k},s}\frac{\partial E_{\mathbf{k},s}}{\partial h_z}\tanh\left(\frac{E_{\mathbf{k},s}}{2T}\right), \tag{B.3}$$

where $s=\pm$, and $E^2_{\mathbf{k},s}=\xi^2_{\mathbf{k}}+h_z^2+\Delta^2+\alpha^2k^2+2s\sqrt{h_z^2(\xi^2_{\mathbf{k}}+\Delta^2)+\alpha^2k^2\xi^2_{\mathbf{k}}}$ gives the quasiparticle excitation spectrum with $\xi_{\mathbf{k}}=\epsilon_{\mathbf{k}}-\mu$ and $\epsilon_{\mathbf{k}}=k^2/(2\,m)$. We again relate g to ϵ_b through the relation $1/g=\sum_{\mathbf{k}}1/(2\epsilon_{\mathbf{k}}+\epsilon_b)$. In the zero-SOC ($\alpha\to 0$) limit, depending on the sign of μ, i.e., respectively when $\mu\gtrless 0$, the spectrum exhibits either two gapless energy rings in $\mathbf{k}$ space at $h_z=\Delta$ or one gapless ring at $h_z=\sqrt{\Delta^2+\mu^2}$. On the other hand, having a finite α allows only a single gapless energy point at $\mathbf{k}=\mathbf{0}$, and it also requires $h_z=\sqrt{\Delta^2+\mu^2}$. Thus, starting with the usual SF phase, increasing h_z from 0 first closes the excitation gap to zero at the critical field $\sqrt{\Delta^2+\mu^2}$, and then reopens it in the topological SF phase.

We solve the self-consistency equations for $h_z=\Delta$ and $h_z=\sqrt{\Delta^2+\mu^2}$, and construct the bulk phase diagrams that are shown in Figs. 2(a), 3(a) and 4, where the population-imbalance parameter $P_z=(N_\uparrow-N_\downarrow)/(N_\uparrow+N_\downarrow)$ is shown as a function of $m\alpha/k_F$. In addition, we show $\Delta=0.005\epsilon_F$ line in the phase diagrams as a guide to the eye for the SF-Normal phase transition boundary that is determined by $\Delta/\epsilon_F\to 0$.

Note that since Δ is assumed to be a constant in Eqs. (B.1)- (B.3), our BCS-BEC meanfield theory excludes the possibility of competing SF phases

that are non-uniform in space. For instance, see Ref. [18] for more accurate phase diagrams of the same system, including the boundary for the phase-separated region. They showed that the phase separation gradually becomes important when ϵ_b/ϵ_F is increased from 0.

References

[1] L.W. Cheuk, A.T. Sommer, Z. Hadzibabic, T. Yefsah, W.S. Bakr, M.W. Zwierlein, Spin-injection spectroscopy of a spin-orbit coupled Fermi gas, Phys. Rev. Lett. 109 (2012), 095302.

[2] R.A. Williams, M.C. Beeler, L.J. LeBlanc, K. Jiménez-García, I.B. Spielman, Raman-induced interactions in a single-component Fermi gas near an s-wave Feshbach resonance, Phys. Rev. Lett. 111 (2013), 095301.

[3] L. Huang, Z. Meng, P. Wang, P. Peng, S.-L. Zhang, L. Chen, D. Li, Q. Zhou, J. Zhang, Experimental realization of a two-dimensional synthetic spin-orbit coupling in ultracold Fermi gases, Nat. Phys. 12 (2016) 540.

[4] Z. Meng, L. Huang, P. Peng, D. Li, L. Chen, Y. Xu, C. Zhang, P. Wang, J. Zhang, Experimental observation of a topological band gap opening in ultracold Fermi gases with two-dimensional spin-orbit coupling, Phys. Rev. Lett. 117 (2016) 235304.

[5] N.Q. Burdick, Y. Tang, B.L. Lev, Long-lived spin-orbit-coupled degenerate dipolar Fermi gas, Phys. Rev. X 6 (2016), 031022.

[6] V. Galitski, I.B. Spielman, Spin-orbit coupling in quantum gases, Nature 494 (7435) (2013) 49.

[7] V.B. Shenoy, J.P. Vyasanakere, Fermions in synthetic non-Abelian gauge potentials: rashbon condensates to novel Hamiltonians, J. Phys. B Atom. Mol. Opt. Phys. 46 (2013) 134009.

[8] J. Zhang, J. Hu, X.J. Liu, H. Pu, Fermi gases with synthetic spin-orbit coupling, Ann. Rev. Cold At. Mol. 2 (2014) 81.

[9] H. Zhai, Degenerate quantum gases with spin-orbit coupling: a review, Rep. Prog. Phys. 78 (2) (2015), 026001.

[10] W. Yi, W. Zhang, X.L. Cui, Pairing superfluidity in spin-orbit coupled ultracold Fermi gases, Sci. China Phys. Mech. Astron. 58 (1) (2015) 1.

[11] Y. Xu, C. Zhang, Topological Fulde-Ferrell superfluids of a spin-orbit coupled Fermi gas, Int. J. Mod. Phys. B 29 (2015) (01), 1530001.

[12] M. Iskin, Spin-orbit-coupling-induced Fulde-Ferrell-Larkin-Ovchinnikov-like Cooper pairing and skyrmion-like polarization textures in optical lattices, Phys. Rev. A 88 (2013), 013631.

[13] M. Serina, D. Loss, J. Klinovaja, Boundary spin polarization as a robust signature of a topological phase transition in Majorana nanowires, Phys. Rev. B 98 (2018), 035419.

[14] F. Dolcini, F. Rossi, Magnetic field effects on a nanowire with inhomogeneous Rashba spin-orbit coupling: spin properties at equilibrium, Phys. Rev. B 98 (2018), 045436.

[15] I.V. Tokatly, B. Bujnowski, F.S. Bergeret, Universal correspondence between edge spin accumulation and equilibrium spin currents in nanowires with spin-orbit coupling, Phys. Rev. B 100 (2019) 214422.

[16] P.-G. de Gennes, Superconductivity of Metals and Alloys, W. A. Benjamin, Inc., 1966.

[17] E. Doko, A.L. Subasi, M. Iskin, Interplay between Rashba spin-orbit coupling and adiabatic rotation in a two-dimensional Fermi gas, Phys. Rev. A 95 (2017), 013601.

[18] X. Yang, S. Wan, Phase diagram of a uniform two-dimensional Fermi gas with spin-orbit coupling, Phys. Rev. A 85 (2012), 023633.

[19] F. Gygi, M. Schlüter, Self-consistent electronic structure of a vortex line in a type-II superconductor, Phys. Rev. B 43 (1991) 7609.

[20] M. Iskin, A.L. Subasi, Stability of spin-orbit coupled Fermi gases with population imbalance, Phys. Rev. Lett. 107 (2011), 050402.